



# Reassessment of the Scale-Determining Equation for Advanced Turbulence Models

David C. Wilcox\*

*DCW Industries, Inc., La Cañada, California*

A comprehensive and critical review of closure approximations for two-equation turbulence models has been made. Particular attention has focused on the scale-determining equation in an attempt to find the optimum choice of dependent variable and closure approximations. Using a combination of singular perturbation methods and numerical computations, this paper demonstrates that: 1) conventional  $k$ - $\epsilon$  and  $k$ - $\omega^2$  formulations generally are inaccurate for boundary layers in adverse pressure gradient; 2) using "wall functions" tends to mask the shortcomings of such models; and 3) a more suitable choice of dependent variables exists that is much more accurate for adverse pressure gradient. Based on the analysis, a two-equation turbulence model is postulated that is shown to be quite accurate for attached boundary layers in adverse pressure gradient, compressible boundary layers, and free shear flows. With no viscous damping of the model's closure coefficients and without the aid of wall functions, the model equations can be integrated through the viscous sublayer. Surface boundary conditions are presented that permit accurate predictions for flow over rough surfaces and for flows with surface mass addition.

## I. Introduction

**D**URING the past 20 years, a great deal of research has focused on the task of devising closure approximations for the long-time-averaged Navier-Stokes equations suitable for predicting properties of turbulent flows. Prior to 1968, virtually all turbulence closure schemes were "incomplete," i.e., their implementation required some advance knowledge about the flowfield under consideration in order to obtain a solution. The best-known incomplete turbulence model is the mixing-length model.<sup>1</sup> This model is incomplete because the appropriate form of the mixing length must be determined empirically for each new application; in general, it cannot be specified a priori.

In 1968, the first Stanford conference<sup>2</sup> on turbulent flows was held to test existing turbulence models against the best experimental data available. The data base was confined to incompressible two-dimensional boundary layers. The competition was won, more or less, by the "incomplete" model of Bradshaw et al.<sup>3</sup>

The trend in turbulence modeling since the first Stanford conference has been toward development of complete models. For clarity, note that the terminology "complete model of turbulence," as used in this paper, means a set of equations that can be used to predict a given turbulent flow with no advance information other than boundary conditions required in order to achieve a solution. The terminology is not intended to imply anything with regard to the range of applicability of the theory.

Over the past 15 years, the most vigorous modeling efforts have been conducted by Donaldson et al.,<sup>4</sup> Launder et al.,<sup>5-6</sup> and Wilcox et al.<sup>7-10</sup> Recognizing the substantial progress the various researchers seemed to be making, the second Stanford conference on turbulent flows was held in 1980 and 1981.<sup>11</sup> This time, however, the scope of the experimental data was expanded tremendously to include complicating effects of compressibility, streamline curvature, surface mass transfer, boundary-layer separation, secondary motions, etc.; that is,

virtually every complicating effect known to man was included if experimental data of reliable quality existed.

From this researcher's viewpoint, results of the second of the two Stanford conferences were at once very encouraging and disappointing. On the one hand, the state-of-the-art has been shown to have advanced dramatically since the first Stanford conference. It was hard to imagine in 1968 that separated flowfields could be routinely predicted with any degree of accuracy just 13 short years later. (Of course, turbulence modelers should receive only part of the credit; magnificent advances in numerical methods, such as those of MacCormack,<sup>12</sup> have played a very important role, to say the least!) On the other hand, although such predictions can be routinely made, obtaining results consistent with measurements is not nearly as routine. Far worse, it was not even clear from the results presented at the second Stanford conference that effects of an adverse pressure gradient on the turbulent boundary layer could be predicted any more accurately than in 1968. Clearly, progress in turbulence modeling has been a bit uneven.

In light of this situation, this study was initiated by taking a modest step backward to review and assess the original closure approximations for the class of turbulence models known as two-equation models; that is, closure being accomplished using the long-time-averaged Navier-Stokes equations and two additional differential equations. The rationale for starting at what would seem to be a very elementary level stems from a key observation made at the second Stanford conference: the greatest amount of uncertainty and controversy over two-equation and higher-order models lies in the scale-determining equation. It is even unclear what the optimum choice of dependent variables is for a two-equation model. As a result of this study, we feel we have found the optimum choice and, based on this choice, we have postulated a new two-equation turbulence model.

Section II summarizes the new model, including arguments that set values of all but two of the closure coefficients appearing in the postulated equations. Section III presents results of a perturbation analysis of the incompressible defect layer, including effects of pressure gradient. Predictions of the new model are compared with those of the Jones-Launder<sup>5</sup> and the Wilcox-Rubesin<sup>10</sup> models. Section IV uses perturbation methods to analyze the viscous sublayer, including effects of surface roughness and surface mass injection. Section V

Presented as Paper 84-0176 at the AIAA 22nd Aerospace Sciences Meeting, Reno, NV, Jan. 9-12, 1984; received Jan. 26, 1987; revision received Nov. 2, 1987. Copyright © American Institute of Aeronautics and Astronautics, Inc., 1987. All rights reserved.

\*President, Associate Fellow AIAA.

includes results of attached boundary-layer computations for boundary layers subjected to adverse pressure gradient, surface mass injection and compressibility, and free shear flows.

## II. Equations of Motion

This section states the postulated equations of motion, including established values of all closure coefficients. Physical interpretations of turbulence field properties are given and, additionally, arguments are presented that have been used in setting values of several of the closure coefficients.

### A. Postulated Equations

For general compressible turbulent fluid flows, the turbulence model equations are written in terms of Favre<sup>13</sup> mass-averaged quantities as follows.

Mass conservation:

$$\frac{\partial \rho}{\partial t} + \frac{\partial}{\partial x_j} (\rho u_j) = 0 \quad (1)$$

Momentum conservation:

$$\frac{\partial}{\partial t} (\rho u_i) + \frac{\partial}{\partial x_j} (\rho u_j u_i) = -\frac{\partial p}{\partial x_i} + \frac{\partial \hat{\tau}_{ij}}{\partial x_j} \quad (2)$$

Mean energy conservation:

$$\frac{\partial}{\partial t} (\rho E) + \frac{\partial}{\partial x_j} (\rho u_j H) = \frac{\partial}{\partial x_j} \left[ u_j \hat{\tau}_{ij} + (\mu + \sigma^* \mu_T) \frac{\partial k}{\partial x_j} - q_j \right] \quad (3)$$

Turbulent mixing energy:

$$\begin{aligned} \frac{\partial}{\partial t} (\rho k) + \frac{\partial}{\partial x_j} (\rho u_j k) &= \tau_{ij} \frac{\partial u_i}{\partial x_j} - \beta^* \rho \omega k \\ &+ \frac{\partial}{\partial x_j} \left[ (\mu + \sigma^* \mu_T) \frac{\partial k}{\partial x_j} \right] \end{aligned} \quad (4)$$

Specific dissipation rate:

$$\begin{aligned} \frac{\partial}{\partial t} (\rho \omega) + \frac{\partial}{\partial x_j} (\rho u_j \omega) &= (\gamma \omega / k) \tau_{ij} \frac{\partial u_i}{\partial x_j} \\ &- \beta \rho \omega^2 + \frac{\partial}{\partial x_j} \left[ (\mu + \sigma \mu_T) \frac{\partial \omega}{\partial x_j} \right] \end{aligned} \quad (5)$$

where  $t$  is time,  $x_i$  position vector,  $u_i$  velocity vector,  $\rho$  density,  $p$  pressure,  $\mu$  molecular viscosity,  $\hat{\tau}_{ij}$  the sum of the molecular and Reynolds stress tensors, and  $q_j$  the sum of the molecular and turbulent heat flux vectors. In Eq. (3), the quantities  $E = e + k + u_i u_i / 2$  and  $H = h + k + u_i u_i / 2$  are total energy and enthalpy, respectively, with  $h = e + p / \rho$ ;  $e$  and  $h$  denote internal energy and enthalpy. Additionally,  $\tau_{ij}$  is the Reynolds stress tensor. The turbulent mixing energy  $k$  and the specific dissipation rate  $\omega$  are needed to define the eddy viscosity  $\mu_T$ , which is given by

$$\mu_T = \gamma^* \frac{\rho k}{\omega} \quad (6)$$

The total viscous stress tensor is given by

$$\hat{\tau}_{ij} = 2\mu \left[ S_{ij} - \frac{1}{3} \frac{\partial u_k}{\partial x_k} \delta_{ij} \right] + \tau_{ij} \quad (7)$$

where, by definition, the mean strain-rate tensor  $S_{ij}$  is

$$S_{ij} = \frac{1}{2} \left[ \frac{\partial u_i}{\partial x_j} + \frac{\partial u_j}{\partial x_i} \right] \quad (8)$$

We invoke the Boussinesq approximation that the Reynolds stress tensor is proportional to the mean strain-rate tensor, that is,

$$\tau_{ij} = 2\mu_T \left[ S_{ij} - \frac{1}{3} \frac{\partial u_k}{\partial x_k} \delta_{ij} \right] - \frac{2}{3} \rho k \delta_{ij} \quad (9)$$

Finally, the heat flux vector  $q_j$  is approximated as

$$q_j = - \left( \frac{\mu}{Pr_L} + \frac{\mu_T}{Pr_T} \right) \frac{\partial h}{\partial x_j} \quad (10)$$

where  $Pr_L$  and  $Pr_T$  are the laminar and turbulent Prandtl numbers, respectively.

Several closure coefficients, namely,  $\beta$ ,  $\beta^*$ ,  $\gamma$ ,  $\gamma^*$ ,  $\sigma$ , and  $\sigma^*$ , appear in Eqs. (1–10). A key objective of this study has been to review typical arguments used in establishing values of such coefficients in a model of this type. In the next subsection and in later sections, the arguments are presented. The values are summarized in the following equations:

$$\begin{aligned} \beta &= 3/40, \quad \beta^* = 9/100, \quad \gamma = 5/9, \quad \gamma^* = 1, \\ \sigma &= 1/2, \quad \sigma^* = 1/2 \end{aligned} \quad (11)$$

Before proceeding to further discussion of the closure coefficients, it is worthwhile to pause and discuss the form of the model equations and the physical meanings of the quantities  $k$  and  $\omega$ . As in other two-equation models of turbulence, the quantity  $k$  represents a measure of the kinetic energy of the turbulence. Whether  $k$  is specifically identified as being the exact kinetic energy of the turbulence or, alternatively, the kinetic energy of the fluctuations in the direction of shear<sup>9</sup> is not critically important. All we require on physical grounds is that  $k$  be proportional to the square of the velocity at which local turbulent mixing occurs. The second quantity introduced in the model,  $\omega$ , is referred to as the specific dissipation rate. Its dimensions are inversely proportional to time, and it is, in fact, the same variable used by this author in all prior turbulence modeling studies. Perhaps the simplest physical interpretation of  $\omega$  is that it is the ratio of the turbulent dissipation rate  $\epsilon$  to the turbulent mixing energy. Alternatively,  $\omega$  is the rate of dissipation of turbulence per unit energy.

As is obvious from inspection of Eq. (4), the equation for  $k$  is modeled directly after the exact, long-time-averaged equation for the turbulent kinetic energy. On this point, the model is consistent with virtually all other two-equation models. The second of the two model equations is similar in form to the equation for  $k$ . Although it adds no rigor to the approach, the equation for  $\omega$  can be regarded as the modeled form of the equation that would result from 1) writing the exact equations for turbulent kinetic energy and dissipation rate and 2) making the formal change of dependent variables defined by

$$\omega = \frac{\epsilon}{(\beta^* k)} \quad (12)$$

The primary difference between the model postulated in this study and the models in this author's prior research is the form of the equation for  $\omega$ . Most notably, past studies have written the equation in terms of the square of  $\omega$ . Interestingly, the first two-equation model in which the variables  $k$  and  $\omega$  were used was postulated by Kolmogorov,<sup>14</sup> and his equation for  $\omega$  was written in terms of  $\omega$  rather than  $\omega^2$ . The reason for our choice will become quite clear in Sec. III, where we analyze model-predicted structure of the defect layer.

### B. Establishing Closure Coefficient Values

In this subsection, we present straightforward arguments from which values of the four closure coefficients  $\beta$ ,  $\beta^*$ ,  $\gamma$ , and  $\gamma^*$  can be established. A review of the arguments generally presented by turbulence model researchers indicates that the following are as physically sound as possible within the context of two-equation turbulence models.

Considering first the coefficient  $\gamma^*$ , we rewrite Eqs. (1-10) in terms of the quantity  $\omega/\gamma^*$ . Inspection of the resulting equations shows that this rescaling of  $\omega$  is equivalent to setting  $\gamma^* = 1$ . Hence, with no loss of generality, we conclude that the value of  $\gamma^*$  is indeed unity.

Next, we turn to the ratio of  $\beta$  to  $\beta^*$ . For decaying homogeneous, isotropic turbulence, Eqs. (4) and (5) simplify to

$$\frac{dk}{dt} = -\beta^* \omega k \quad \text{and} \quad \frac{d\omega}{dt} = -\beta \omega^2 \quad (13)$$

from which the asymptotic solution for  $k$  is readily found to be

$$k \sim t^{-\beta^*/\beta} \quad (14)$$

Experimental observations indicate that  $k \sim t^{-6/5}$  for decaying, homogeneous, isotropic turbulence, which implies that  $\beta^*/\beta = 6/5$ .

Values for the coefficients  $\gamma$  and  $\beta^*$  can be established by examining the so-called "wall layer." The wall layer is defined as the portion of the boundary layer far enough from the surface to render molecular viscosity negligible relative to eddy viscosity, yet close enough for convective effects to be negligible relative to the rate at which the turbulence is being created and destroyed. In the limiting case of an incompressible constant-pressure boundary layer, defining  $\nu_T = \mu_T/\rho$ , Eqs. (1-10) simplify to

$$\begin{aligned} 0 &= \frac{\partial}{\partial y} \left[ \nu_T \frac{\partial u}{\partial y} \right] \\ 0 &= \nu_T \left[ \frac{\partial u}{\partial y} \right]^2 - \beta^* \omega k + \sigma^* \frac{\partial}{\partial y} \left[ \nu_T \frac{\partial k}{\partial y} \right] \\ 0 &= \gamma \left[ \frac{\partial u}{\partial y} \right]^2 - \beta \omega^2 + \sigma \frac{\partial}{\partial y} \left[ \nu_T \frac{\partial \omega}{\partial y} \right] \end{aligned} \quad (15)$$

We seek the conditions under which these simplified equations yield a solution consistent with the law of the wall, i.e., velocity varying linearly with the logarithm of distance from the surface. As can easily be verified, Eqs. (15) possess a solution consistent with the law of the wall, namely,

$$u = \frac{u_\tau}{\kappa} \ln \left[ \frac{u_\tau y}{\nu} \right], \quad k = \frac{u_\tau^2}{\sqrt{\beta^*}}, \quad \omega = \frac{u_\tau}{(\sqrt{\beta^*} \kappa y)} \quad (16)$$

where  $u_\tau$  is the conventional friction velocity and  $\kappa$  is von Kármán's constant. There is one constraint imposed in the solution to Eqs. (15): a unique relation exists between the implied value of von Kármán's constant and the various closure coefficients. Specifically, the following equation must hold.

$$\gamma = \frac{\beta}{\beta^*} - \frac{\sigma \kappa^2}{\sqrt{\beta^*}} \quad (17)$$

Additionally, note that the Reynolds shear stress  $\tau$  is constant in the wall layer and is equal to  $u_\tau^2$ . Inspection of Eq. (16) shows that this implies  $\tau/k = \sqrt{\beta^*}$  in the wall layer. A variety of experimental measurements<sup>15</sup> indicate that the ratio of  $\tau$  to  $k$  is about 3/10 in the wall layer. Thus, the predicted wall-layer solution is consistent with experimental observations, provided  $\beta^* = 9/100$ .

In summary, the arguments presented in this subsection are sufficient to uniquely set the values of  $\gamma^*$ ,  $\beta^*$ , and  $\beta$ . Also, Eq. (17) determines  $\gamma$  in terms of the as-yet undetermined value of  $\sigma$ . As a by-product of analysis in the next section, the values of  $\sigma$  and  $\sigma^*$  will be established.

### III. Defect-Layer Analysis

In this section, we use singular perturbation methods to analyze model-predicted structure of the classical defect layer. The analysis presented is a generalization of that done by Wilcox and Traci.<sup>9</sup> In contrast to the Wilcox and Traci analysis, effects of pressure gradient have been included. Additionally, the analysis has been done for three turbulence models: the model postulated in Eqs. (1-10), the Wilcox-Rubesin<sup>10</sup> model, and the Jones-Launder<sup>5</sup> model. First, we review details of the perturbation solution procedure. Next, we compare solutions for the three models in the absence of pressure gradient. Then, effects of pressure gradient are studied for the three models. Finally, we justify the values chosen for  $\sigma$  and  $\sigma^*$ .

#### A. Perturbation Solution

In the past, the only detailed analyses of the defect layer for any turbulence model have been those of Bush and Fendell<sup>16</sup> (for the mixing-length model) and Wilcox and Traci (for a  $k-\omega^2$  model). In neither case were effects of pressure gradient delineated. In this section, we extend the Wilcox-Traci analysis to include pressure gradient.

To study the defect layer, we confine our analysis to incompressible flow and we seek a perturbation solution. The expansion proceeds in terms of the ratio of friction velocity to the boundary-layer-edge velocity  $u_\tau/U_e$  and the dimensionless vertical coordinate  $\eta$ , defined by

$$\eta = \frac{u_\tau y}{U_e \delta^*} \quad (18)$$

where  $\delta^*$  is displacement thickness. For the sake of brevity, we confine details of the expansion procedure to the Appendix. It is instructive to note that the velocity is given by

$$\frac{u}{U_e} = 1 - \left( \frac{u_\tau}{U_e} \right) U_1(\eta) + \dots \quad (19)$$

which, to order  $u_\tau/U_e$ , can be rewritten as

$$\frac{(U_e - u)}{u_\tau} = f\left(\frac{y}{\Delta}\right), \quad \Delta = \frac{U_e \delta^*}{u_\tau} \quad (20)$$

The coordinates appearing in Eq. (20) are the classical defect-layer coordinates. Additionally, it is important to note that pressure gradient appears in the equations of motion in dimensionless form as

$$\beta_T = \delta^* (dp/dx) / \tau_w \quad (21)$$

where  $\tau_w$  is the surface shear stress. Coles and Hirst<sup>2</sup> refer to  $\beta_T$  as the equilibrium parameter.

In order to solve the defect-layer equations, we have used an improved version of the implicit time-marching program developed by Wilcox and Traci. That is, we add unsteady terms to each of the equations of motion, make an educated guess at the solution, and integrate over time until the solution displays negligible temporal variation.

#### B. Flat-Plate Boundary Layer

Figure 1a compares numerical predictions of the three models with corresponding experimental data of Wieghardt as tabulated by Coles and Hirst.<sup>2</sup> (Note that, in the new-model computation, we use  $\sigma = \sigma^* = 1/2$ ; we defer any further discussion of the appropriate values to Sec. IIID.) The experi-

mental data presented are those at the highest Reynolds number for which data are reported. This is consistent with the defect-layer solution that is formally valid for very large Reynolds number. Numerical results are shown for three models: the new ( $k-\omega$ ) model, the Wilcox-Rubesin ( $k-\omega^2$ ) model, and the Jones-Launder ( $k-\epsilon$ ) model.

As shown, all three models predict velocity profiles that differ from measured values by no more than about 3% of scale. Interestingly, the new model shows the smallest differences from the Wieghardt data. Additionally, skin friction  $C_f$  can be inferred from the defect-layer solution (see Appendix). Corresponding computed and measured values are summarized in the insert on Fig. 1a; the largest difference is less than 3%. Thus, based on analysis of the constant-pressure defect layer, there is little difference among the three models.

### C. Effects of Pressure Gradient

Turning now to the effect of pressure gradient, we have computed defect-layer solutions for the equilibrium parameter  $\beta_T$ , ranging from  $-0.5$  to  $+9.0$ , where positive  $\beta_T$  corresponds to an adverse pressure gradient. The choice of this range of  $\beta_T$  has been dictated by the requirement of the perturbation solution that  $\beta_T$  be constant. This is as wide a range as we have been able to find for which experimental data have been taken with  $\beta_T$  more or less constant.

Figure 1c compares computed wake strength  $\tilde{\pi}$  with values inferred by Coles and Hirst<sup>2</sup> from experimental data. For the sake of clarity, note that the wake strength appears in Coles' composite law-of-the-wall/wake profile,

$$\frac{u}{u_\tau} = \frac{1}{\kappa} \ln \left[ \frac{u_\tau y}{\nu} \right] + B + \frac{2\pi}{\kappa} \sin^2 \left[ \frac{\pi}{2} \frac{y}{\delta} \right] \quad (22)$$

Inspection of Fig. 1c reveals provocative differences among the three models. Most notably, the new model yields wake

strengths closest to values inferred from data over the complete range considered. Consistent with predictions of Chambers and Wilcox,<sup>17</sup> the Jones-Launder model exhibits the largest differences, with predicted wake strength 50–100% lower than inferred values when  $\beta_T$  is as small as 2!

Figure 1b compares computed velocity profiles with experimental data of Clauser<sup>2</sup> for  $\beta_T = 8.7$ . As with the constant-pressure case, computed and measured skin friction are included in the insert. Consistent with the wake-strength predictions, the new model yields a velocity profile and skin friction closest to measurements, whereas the Jones-Launder model shows the greatest differences. The Wilcox-Rubesin profile and skin friction lie about midway between those of the other two models.

The explanation of the Jones-Launder model's poor performance for adverse pressure gradient can be developed from inspection of the asymptotic behavior of solutions as  $\eta \rightarrow 0$ . For the three models tested, the velocity behaves as

$$(U_e - u)/u_\tau \sim -\kappa^{-1} \ln \eta + A - \beta_T C \eta \ln \eta + \dots \quad \text{as } \eta \rightarrow 0 \quad (23)$$

where Table 1 summarizes the constants  $A$  and  $C$ . Note that while the coefficient  $A$  is determined as part of the solution (from the integral constraint that mass be conserved), the coefficient  $C$  follows directly from the limiting form of the solution as  $\eta \rightarrow 0$ . As seen from Table 1,  $C$  is largest for the Jones-Launder model and smallest for the new model. The presence of the  $\eta \ln \eta$  term gives rise to the inflection in the velocity profile as  $\eta \rightarrow 0$  that is most pronounced for the Jones-Launder model. In terms of turbulence properties, the turbulence length scale,  $\ell = k^{1/2}/\omega$ , behaves according to

$$\ell \sim \beta_T^{1/2} \kappa \eta [1 + \beta_T L \eta \ln \eta + \dots] \quad \text{as } \eta \rightarrow 0 \quad (24)$$

Table 1 also includes the coefficient  $L$  for each model. Again, we see that the  $\eta \ln \eta$  term is largest for the Jones-Launder model and smallest for the new model. Thus, in the presence of adverse pressure gradient, the Jones-Launder turbulence length scale tends to be too large in the near-wall region. Note, of course, that this shortcoming is not evident in the constant-pressure case, which has  $\beta_T = 0$ .

The manner in which the new model achieves smaller values of  $\ell$  than the Jones-Launder model can be seen by changing dependent variables. That is, starting with the  $k-\omega$  formulation, defining  $\epsilon \equiv \beta^* \omega k$  and  $\nu_T \equiv k/\omega$ , we can deduce the following incompressible equation for  $\epsilon$  implied by the new model:

$$\begin{aligned} \frac{d\epsilon}{dt} = & (1 + \gamma)k \left[ \frac{\partial u}{\partial y} \right]^2 - \left( 1 + \frac{\beta}{\beta^*} \right) \frac{\epsilon^2}{k} \\ & + \frac{\partial}{\partial y} \left[ \sigma \nu_T \frac{\partial \epsilon}{\partial y} \right] - 2\sigma \nu_T \frac{\partial k}{\partial y} \left[ \frac{\partial(\epsilon/k)}{\partial y} \right] \end{aligned} \quad (25)$$

All terms except the last one on the right-hand side of Eq. (25) are identical in form to those of the Jones-Launder model (see Appendix). The last term is negligibly small as  $\eta \rightarrow 0$  for constant-pressure boundary layers because  $k \rightarrow \text{constant}$  as  $\eta \rightarrow 0$ . However,  $\partial k / \partial y$  is nonvanishing when  $\beta_T \neq 0$  and  $\partial(\epsilon/k) / \partial y$  generally is quite large as  $\eta \rightarrow 0$ . The net effect of this additional term is to suppress the rate of increase of  $\ell$  close to the surface.

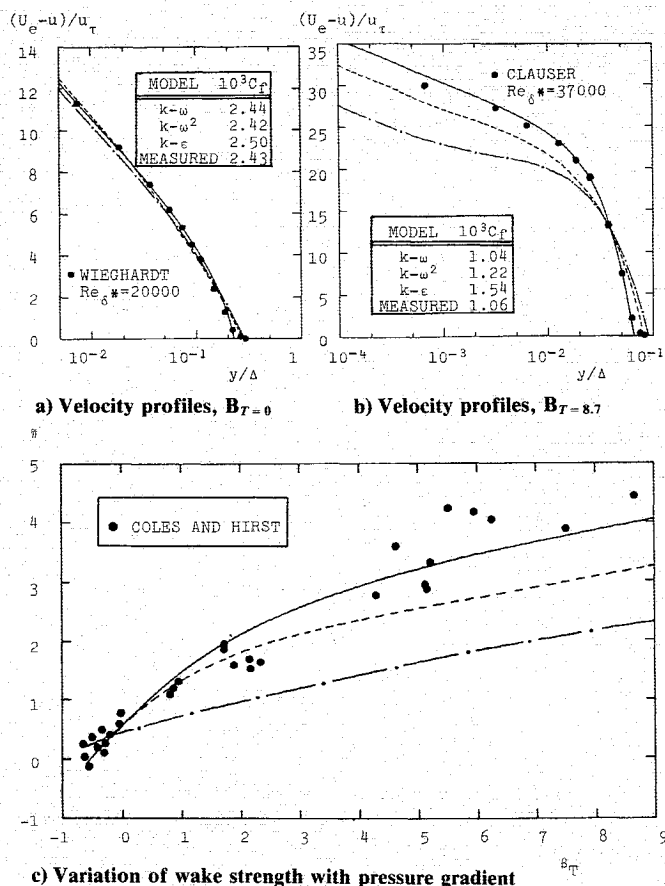


Fig. 1 Comparison of computed and measured defect-layer properties: —  $k-\omega$  model; ---  $k-\omega^2$  model; - - -  $k-\epsilon$  model.

Table 1 Summary of coefficients  $A$ ,  $C$ , and  $L$  in Eqs. (23) and (24) for  $\beta_T = 9$

Model	$A$	$C$	$L$
New	13.1	10.6	-19.8
Wilcox-Rubesin	9.8	23.4	-32.6
Jones-Launder	5.4	54.8	-61.1

As a final comment, note that all of the computations have used the model-predicted behavior [e.g., Eqs. (23) and (24)] as "wall-function" type of boundary conditions for  $\eta \rightarrow 0$ . Using other empirical wall functions presumably would improve the Jones-Launder predictions. However, the asymptotic behavior (e.g., inflected velocity profile) inherent in the model ultimately must prevail at high Reynolds number if the point of application of the wall functions remains constant at, say,  $y^+ = 80$ . To understand this point, one need only note that, by definition,  $\eta$  is related to  $y^+$  by

$$\eta = \frac{y^+}{(U_e \delta^*/\nu)} \quad (26)$$

Hence, suppressing the asymptotic behavior inherent in the model requires using wall functions to increasingly larger values of  $y^+$  as Reynolds number increases.

#### D. Establishing Closure Coefficient Values

Unlike the four closure coefficients discussed in Sec. IIB, we have been unable to find satisfactory arguments to establish the values of  $\sigma$  and  $\sigma^*$  before performing any numerical computations. However, we have found from numerical experimentation that the computed variation of  $\tilde{\pi}$  with  $\beta_T$  (Fig. 1c) seems to match experimental results most faithfully when we use  $\sigma = \sigma^* = 1/2$ . Effects of departures from this pair of values are so pronounced, in fact, that our computations seem to indicate that  $\sigma = \sigma^* = 1/2$  represents a saddle point in closure-coefficient space! Thus, we conclude that  $\sigma$  and  $\sigma^*$  are equal and that the most appropriate value is  $1/2$ .

### IV. Sublayer Analysis

In order to facilitate integration of the model equations through the viscous sublayer, we must, at a minimum, have molecular diffusion terms in the equations of motion. Potentially, we might also have to allow the various closure coefficients to be functions of viscosity as well. In this section, we use perturbation methods to analyze viscous sublayer structure predicted by the new model, including effects of surface roughness and surface mass injection. Note that we confine our analysis to the new model because results of Sec. III indicate that it is superior to the other models considered.

#### A. Perturbation Solution

Considering the incompressible constant-pressure case, convective terms are negligible in the sublayer; thus, the equations of motion for the new model (with molecular diffusion included) simplify to

$$u_T^2 = (\nu + \nu_T) \frac{du}{dy} \quad (27)$$

$$0 = \nu_T \left[ \frac{du}{dy} \right]^2 - \beta^* \omega k + \frac{d}{dy} \left[ (\nu + \sigma^* \nu_T) \frac{dk}{dy} \right] \quad (28)$$

$$0 = \gamma \left[ \frac{du}{dy} \right]^2 - \beta \omega^2 + \frac{d}{dy} \left[ (\nu + \sigma \nu_T) \frac{d\omega}{dy} \right] \quad (29)$$

Five boundary conditions are needed for this fifth-order system, two of which follow from matching to the law of the wall as  $y^+ \rightarrow \infty$ :

$$k \rightarrow \frac{u_T^2}{\sqrt{\beta^*}} \quad \text{and} \quad \omega \rightarrow \frac{u_T}{(\sqrt{\beta^*} \kappa y)} \quad \text{as } y^+ \rightarrow \infty \quad (30)$$

where  $y^+ \equiv u_T y / \nu$ . Two more boundary conditions follow from "no slip" at the surface, which implies that  $u$  and  $k$  vanish at  $y = 0$ . Thus,

$$u = k = 0 \quad \text{at} \quad y^+ = 0 \quad (31)$$

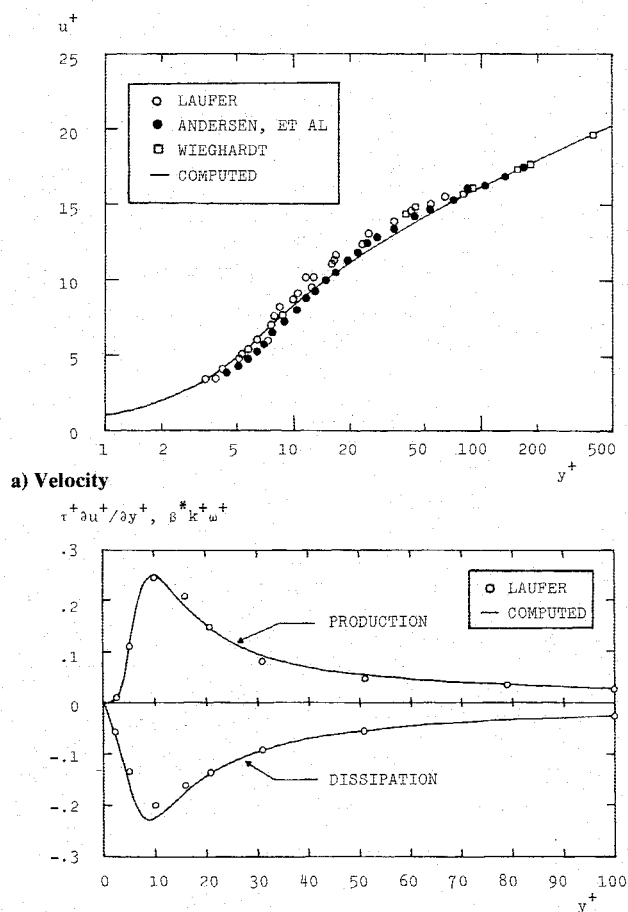


Fig. 2 Comparison of computed and measured sublayer properties for a perfectly smooth surface.

The final condition is similar to that deduced in earlier studies,<sup>8-10</sup> where we have found that, for perfectly smooth surfaces, molecular diffusion and dissipation balance in Eq. (29), and this leads to

$$\omega \rightarrow \frac{6\nu}{(\beta y^2)} \quad \text{as } y^+ \rightarrow 0 \quad (32)$$

More general boundary conditions for rough surfaces and for surfaces with mass injection will be devised in Secs. IVB and IVC. For now, we focus on the perfectly smooth surface.

As part of the solution to Eqs. (27-32), we obtain the constant in the law of the wall,  $B$ , where the velocity,  $u^+ \equiv u/u_T$ , asymptotes to

$$u^+ \rightarrow \frac{1}{\kappa} \ln y^+ + B \quad \text{as } y^+ \rightarrow \infty \quad (33)$$

As with the defect layer, we solve the sublayer equations by 1) adding unsteady terms to the left-hand sides of Eqs. (28) and (29), 2) making an initial guess at the solution, and 3) using an implicit, time-marching, second-order-accurate program to generate the long-time solution in which the unsteady terms tend to zero. The velocity is computed at each time step using the fourth-order Runge-Kutta method. The program used is an improved version of that developed in the study by Wilcox and Traci.<sup>9</sup>

Using this program, we find that Eqs. (27-32) predict the smooth-wall value of  $B$  as

$$B = \lim_{y^+ \rightarrow \infty} \left[ u^+ - \frac{1}{\kappa} \ln y^+ \right] = 5.1 \quad (34)$$

That this value is well within the scatter of measured values of  $B$  strongly suggests that no further viscous modifications are needed.

Figure 2a compares computed and measured<sup>2,18,19</sup> sublayer velocity profiles. As shown, computed velocities generally fall within experimental data scatter. In Fig. 2b, we compare computed and measured<sup>18</sup> turbulence production and dissipation terms. Again, predictions fall well within experimental error bounds.

Perhaps the only deficiency of predicted smooth-surface sublayer structure is that, very near the surface, the model predicts

$$k \sim y^{3.23} \quad \text{as} \quad y \rightarrow 0 \quad (35)$$

By contrast, the Wilcox-Rubesin model predicts that  $k \sim y^4$ , which suggests that  $k \sim \langle v'^2 \rangle$ , a point this researcher has made<sup>9</sup> as a more plausible interpretation than saying that  $k$  is the kinetic energy of the turbulence. By letting the closure coefficient  $\beta^*$  increase as a function of turbulent Reynolds number,  $Re_T \equiv k/(\omega\nu)$ , it is possible to force either  $k \sim y^4$  or  $k \sim y^2$ , but then we find that to recover  $B \approx 5$ , at least two other closure coefficients must vary with  $Re_T$ . Such additional complexity is pointless in light of Fig. 2.

### B. Rough-Wall Analysis

A key advantage of the  $k$ - $\omega^2$  and  $k$ - $\omega$  formulations over the  $k$ - $\epsilon$  formulation is the fact that  $\omega$ -oriented equations possess solutions in which the value of  $\omega$  may be arbitrarily specified at the surface.<sup>17</sup> This is an advantage because it provides a natural way to incorporate effects of surface roughness through surface boundary conditions. This feature of the equations was originally recognized by Saffman.<sup>20</sup>

If we now rewrite the surface boundary condition [Eq. (32)] on  $\omega$  as

$$\omega = \frac{u_\tau^2}{\nu} S_R \quad \text{at} \quad y = 0 \quad (36)$$

we can generate sublayer solutions for arbitrary  $S_R$ , including the limiting cases  $S_R \rightarrow 0$  and  $S_R \rightarrow \infty$ .

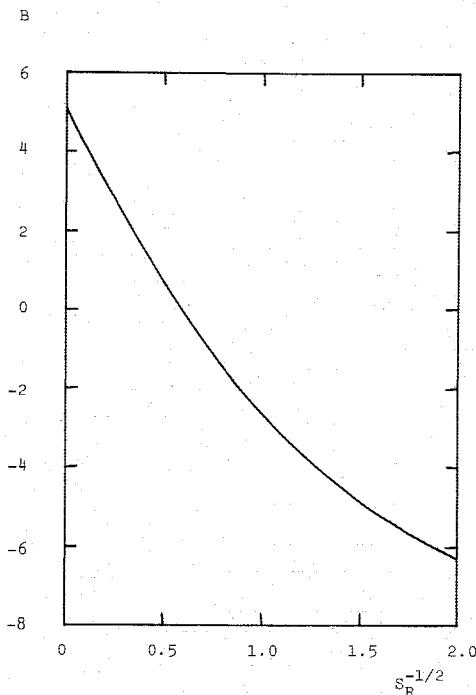


Fig. 3 Computed variation of the constant in the law of the wall,  $B$ , with the surface value of the specific dissipation rate.

Figure 3 shows the computed value of  $B$  for a wide range of values of  $S_R$ . As shown, in the limit  $S_R \rightarrow \infty$ ,  $B$  tends to 5.1. In the limit  $S_R \rightarrow 0$ , an excellent correlation of the numerical predictions is given by

$$B \rightarrow 8.4 + \frac{1}{\kappa} \ln \frac{S_R}{100} \quad \text{as} \quad S_R \rightarrow 0 \quad (37)$$

By experimental means, as summarized by Schlichting,<sup>21</sup> Nikuradse found that for flow over very rough surfaces,

$$B \rightarrow 8.5 + \frac{1}{\kappa} \ln \frac{1}{k_R^+}, \quad k_R^+ = \frac{u_\tau k_R}{\nu} \quad (38)$$

where  $k_R$  is the average height of sand-grain roughness elements. (Note that, in our computations, we use  $\kappa = 0.41$ , whereas Nikuradse used  $\kappa = 0.40$ .) Thus, if we make the correlation

$$S_R = \frac{100}{k_R^+} \quad \text{for} \quad k_R^+ \gg 1 \quad (39)$$

then Eqs. (37) and (38) are nearly identical. Figure 4 compares computed velocity profiles with the analytical fit obtained by using Eqs. (37) and (38) in the law of the wall, that is,

$$u^+ = \frac{1}{\kappa} \ln \frac{y}{k_R} + 8.4 \quad (40)$$

for three of the computations. The correlation is nearly exact. The most remarkable fact about this correlation is that Eq. (40) is the form the law of the wall assumes for flow over "completely rough" surfaces, including the value of the additive constant (8.4 and 8.5 differ by 1%).

By making a qualitative argument based on flow over a wavy wall, Wilcox and Chambers<sup>22</sup> have shown that, for small roughness heights, we should expect to have

$$S_R \sim \left( \frac{1}{k_R^+} \right)^2 \quad \text{as} \quad k_R^+ \rightarrow 0 \quad (41)$$

Comparison with Nikuradse's data shows that the following correlation between  $S_R$  and  $k_R^+$  will reproduce measured effects of sand-grain roughness for values of  $k_R^+$  up to about 400.

$$S_R = \begin{cases} \left( \frac{50}{k_R^+} \right)^2, & k_R^+ < 25 \\ \frac{100}{k_R^+}, & k_R^+ \geq 25 \end{cases} \quad (42)$$

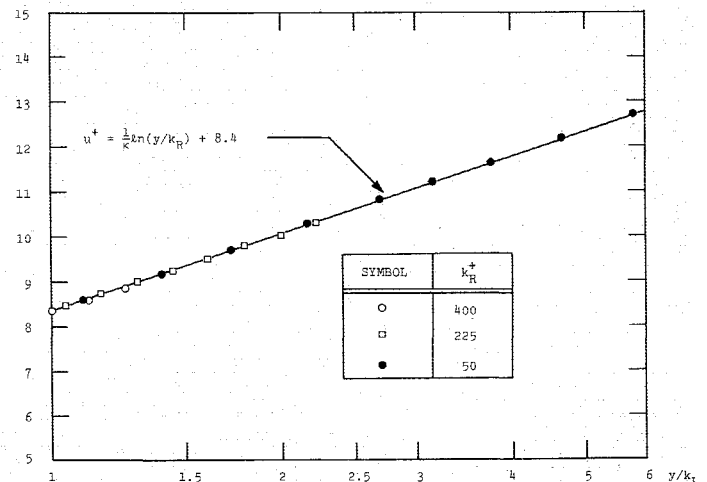


Fig. 4 Comparison of computed and measured sublayer velocity profiles for "completely rough" surfaces.



### C. Effects of Surface Mass Injection

For boundary layers with surface mass injection, the introduction of an additional velocity scale ( $v_w$  = normal flow velocity at the surface) suggests that the scaling for  $\omega$  at the surface may differ from Eq. (36). Andersen et al.<sup>19</sup> provide further evidence that the specific-dissipation-rate boundary condition must be revised when mass injection is present by showing, from correlation of their experimental data, that both  $\kappa$  and  $B$  are functions of  $v_w^+ = v_w/\bar{u}_\tau$ . Because our rough-surface computations of the preceding subsection show that the value of  $B$  is strongly affected by the surface value of the specific dissipation rate, this suggests that the surface value of  $\omega$  will depend in some manner on  $v_w$ . Examination of the limiting form of the model equations for  $y^+ \rightarrow \infty$  (i.e., the "wall-layer" in Sec. IIB) shows immediately that the effective von Kármán "constant" varies with  $v_w^+$  according to

$$\tilde{\kappa} = \frac{\kappa}{1 + \tilde{\epsilon} v_w^+} \quad (43)$$

where  $\tilde{\epsilon}$  is given by

$$\tilde{\epsilon} = 3.11 + 0.61 \ln y^+ \quad (44)$$

The variation of  $\tilde{\kappa}$  predicted in Eqs. (43) and (44) is consistent with the data of Andersen et al. Including appropriate convective terms in Eqs. (27–29), we have performed sublayer computations for the cases experimentally documented by Andersen et al. In each case, the surface value of  $\omega$  has been given by

$$\omega = \frac{u_\tau^2}{\nu} S_B \quad \text{at} \quad y = 0 \quad (45)$$

and the value of  $S_B$  has been varied until optimum agreement between measured and computed velocity profiles is achieved. The final correlation between  $S_B$  and  $v_w^+$  is given in analytical form as

$$S_B = \frac{20}{v_w^+ (1 + 5v_w^+)} \quad (46)$$

Figure 5 displays the level of agreement between theory and experiment using Eqs. (45) and (46). This concludes our formulation of the new turbulence model and attending surface boundary conditions.

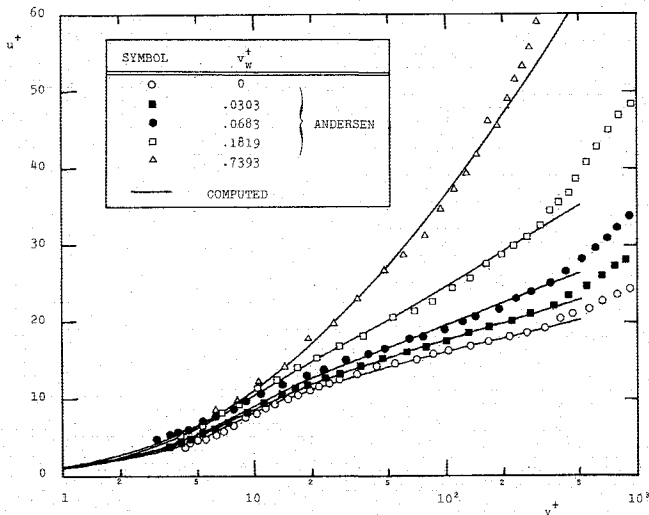


Fig. 5 Comparison of computed and measured sublayer velocity profiles for boundary layers with surface mass injection.

### V. Numerical Applications

The purpose of this section is to apply the new model to several well-documented turbulent boundary layers, including effects of adverse pressure gradient, surface mass injection, and compressibility, and to free shear flows. All boundary-layer computations have been done with a second-order-accurate boundary-layer program, EDDYBL,<sup>23</sup> based on the Blottner<sup>24</sup> variable-grid method and the algorithm developed by Wilcox<sup>25</sup> to permit large streamwise steps. The free shear flow computations have been done with the same numerical procedure implemented to solve the sublayer equations in Sec. IV.

#### A. Boundary Conditions

For boundary-layer computations, we must specify boundary conditions at the surface ( $y = 0$ ) and at the edge of the layer ( $y = \delta$ ). At the surface, we impose the no-slip condition, which gives the following:

$$u = k = 0 \quad \text{at} \quad y = 0 \quad (47)$$

For compressible flows, we specify either surface temperature  $T_w$  or surface heat flux  $q_w$ , so that the enthalpy boundary condition for a calorically perfect gas becomes

$$h = \frac{T_w}{C_p} \quad \text{or} \quad \frac{\partial h}{\partial y} = \frac{-Pr_L C_p q_w}{\mu_w} \quad \text{at} \quad y = 0 \quad (48)$$

where  $C_p$  is specific heat at constant pressure and subscript  $w$  denotes surface ( $y = 0$ ) value. For the compressible flow

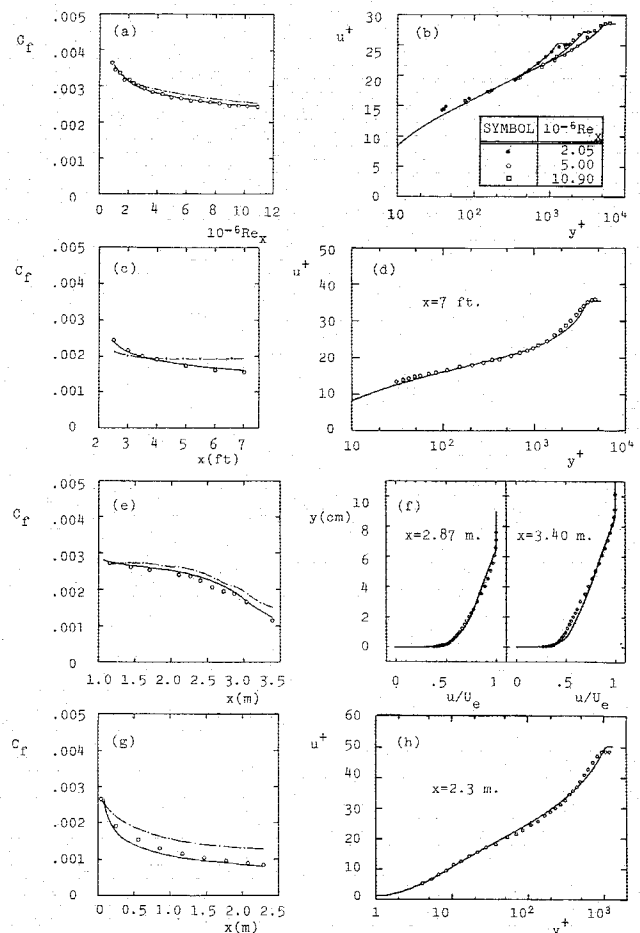


Fig. 6 Comparison of computed and measured skin-friction and velocity profiles for incompressible boundary layers: —  $k$ - $\omega$  model; ---  $k$ - $\epsilon$  model;  $\circ$  measured.

computations of Sec. VB, we assume that our fluid is air so that  $Pr_L = 0.72$ , and the value used for  $Pr_T$  is 8/9. Finally, for perfectly smooth surfaces with no surface mass injection, we require that

$$v = 0 \quad \text{and} \quad \omega \rightarrow \frac{6\nu_w}{\beta y^2} \quad \text{as} \quad y \rightarrow 0 \quad (\text{no mass injection}) \quad (49)$$

For the computation with surface mass injection (Sec. VB), the surface conditions satisfied by  $v$  and  $\omega$  are given by

$$v = v_w \quad \text{and} \quad \omega = \frac{u_\tau^2}{\nu_w} S_B \quad \text{at} \quad y = 0 \quad (\text{with mass injection}) \quad (50)$$

where the dimensionless coefficient  $S_B$  is defined in terms of the blowing rate parameter  $v_w^+ = v_w/u_\tau$  by Eq. (46).

The manner in which the surface boundary condition on  $\omega$  is implemented when mass addition is present is straightforward. For the perfectly smooth surface, the method used is less obvious and requires special care. As indicated in Eq. (49), we must make sure  $\omega$  approaches the correct asymptotic form as  $y \rightarrow 0$ . If proper care is not taken, the near-wall velocity profile is distorted which, in turn, distorts the entire boundary layer. Note that the singular behavior of  $\omega$  is consistent with the physics of turbulence, which dictates that there are rapidly decaying small eddies close to solid boundaries. This means that the time scale for decay, proportional to the reciprocal of  $\omega$ , must approach 0 as  $y \rightarrow 0$ .

In order to achieve the proper limiting form, the boundary-layer program uses Eq. (49) for all points up to  $y^+ = u_\tau y/\nu_w = 2.5$  rather than attempting to solve the differential equation for  $\omega$  directly. This procedure is very accurate, provided the mesh point closest to the surface lies below  $y^+ = 1$  and that at least 5 mesh points lie between  $y^+ = 0$  and  $y^+ = 2.5$ . Note that Eq. (49) is the *exact solution* to Eq. (5) in the limit  $y^+ \rightarrow 0$ , and using it to define  $\omega$  for the mesh points closest to the surface is done to guarantee numerical accuracy. The procedure should not be confused with the use of wall functions.

In addition to specifying surface boundary conditions, values of the dependent variables must also be specified at the edge of the boundary layer. Ideally, we would like to implement "zero-gradient" boundary conditions at the boundary-layer edge. Although such conditions are "clean" from a theoretical point of view, they are undesirable from a numerical point of view. That is, the conditions we have used in past applications are of the Neumann type, whereas "zero-gradient" conditions are of the Dirichlet type. Almost universally, convergence of iterative numerical schemes (EDDYBL uses an iterative scheme) is much slower with Dirichlet conditions than with Neumann conditions.

In order to resolve this apparent dilemma, we appeal directly to the equations of motion. Beyond the boundary-layer edge, we have vanishing normal gradients, so that the equations for  $k$  and  $\omega$  simplify to the following:

$$U_e \frac{dk_e}{dx} = -\beta^* \omega_e k_e \quad (51)$$

$$U_e \frac{d\omega_e}{dx} = -\beta \omega_e^2 \quad (52)$$

where subscript  $e$  denotes the value at the boundary-layer edge. The solution to Eqs. (51) and (52) can be obtained by simple quadrature, independently of integrating the equations of motion through the boundary layer. Once  $k_e$  and  $\omega_e$  are determined from Eqs. (51) and (52), it is then possible to specify Neumann-type boundary conditions that guarantee zero normal gradients.

## B. Boundary-Layer Applications

We turn now to application of the new model equations to a total of four incompressible boundary layers and to the

compressible constant-pressure (flat-plate) boundary layer. First, we apply the model to the incompressible flat-plate case. The next two applications are to boundary layers in an adverse pressure gradient. The final incompressible application is for a boundary layer with surface mass injection. We conclude with application of the model to the compressible flat-plate boundary layer with and without heat transfer for Mach numbers 0–5. Numerical details of the computations are given by Wilcox.<sup>26</sup>

### Incompressible Flat-Plate Boundary Layer

The first application is for the constant-pressure incompressible boundary layer. Although this application does not provide a severe test of the new model, it is nevertheless necessary to be sure the boundary-layer program has been coded properly. Also, the new model would be of little use as a predictive tool if it were inaccurate for the simplest of all boundary layers.

The computation begins at a plate-length Reynolds number  $Re_x$  of  $1 \cdot 10^6$  and continues to an  $Re_x$  of  $10.9 \cdot 10^6$ . Figures 6a and 6b compare computed and measured<sup>2</sup> skin-friction and velocity profiles, respectively. As shown in Fig. 6a, computed skin friction virtually duplicates corresponding measurements for the entire range of Reynolds numbers considered. Figure 6b shows that differences between computed and measured velocity profiles are no more than 3% of scale for the three Reynolds numbers indicated. Thus, it comes as no great surprise that the new model is quite accurate for the flat-plate boundary layer. Skin-friction results<sup>17</sup> for the  $k$ - $\epsilon$  model are included in Fig. 6a. Note that, as predicted in the defect-layer analysis of Sec. III, computed  $C_f$  is about 3% higher than measured.

### Incompressible Boundary Layers with Adverse Pressure Gradient

We consider two boundary layers with adverse pressure gradient. The first case has a moderate adverse pressure gradient, the experimental data being those of Bradshaw<sup>2</sup> (case 3300). The second case has increasingly adverse pressure gradient, the experimental data being those of Samuel and Joubert<sup>11</sup> (flow 0141).

For the Bradshaw case, streamwise distance extends from  $x = 2.5$  to 7.0 ft, corresponding to an increase in  $Re_x$  from about  $2 \cdot 10^6$  to about  $4 \cdot 10^6$ . Figures 6c and 6d compare computed and measured skin friction and a velocity profile. Inspection of both graphs shows that differences between theory and experiment nowhere exceed 5% for this flow. Figure 6c includes  $k$ - $\epsilon$  results obtained by Chambers and Wilcox;<sup>17</sup> computed  $C_f$  exceeds measured values by as much as 20%. Because the equilibrium parameter  $\beta_T \approx 2$  for this flow, the poor results for the  $k$ - $\epsilon$  model are unsurprising.

In the Samuel-Joubert case, we integrate from  $x = 1$  to 3.40 m, corresponding to an  $Re_x$  range of about  $2 \cdot 10^6$ – $4 \cdot 10^6$ . Figures 6e and 6f compare computed and measured skin-friction and two velocity profiles for this flow. Computed and measured skin friction differ by less than 5% of scale. Velocity profiles at  $x = 2.87$  m are within 5% whereas those at  $x = 3.40$  m differ by no more than 9%. Since  $\beta_T$  exceeds 9 toward the end of the computation, the poor performance<sup>27</sup> of the  $k$ - $\epsilon$  model shown in Fig. 6e (computed  $C_f$  exceeds measured values by as much as 35%) is again consistent with the defect-layer analysis of Sec. III.

### Incompressible Boundary Layer with Surface Mass Injection

As the final incompressible application of the model, we consider a boundary layer with surface mass injection. The case considered was included in the second Stanford conference<sup>12</sup> (flow 0241), and data for the flow were taken by Andersen et al.<sup>19</sup> The surface mass injection rate  $v_w$  is 0.00375  $U_e$ , where  $U_e$  is the constant boundary-layer-edge velocity, i.e., the flow has constant pressure. Figures 6g and 6h compare computed and measured skin-friction and velocity profiles, respectively. As shown, computed and measured skin



friction differ by less than 4% of scale whereas computed and measured velocity profiles are within 3% of each other. Although this flow has zero pressure gradient, corresponding skin friction predicted<sup>11</sup> by the  $k-\epsilon$  model is as much as 50% higher than measured, probably because the wall functions used by Rodi in this computation are inadequate for flows with mass injection.

#### Compressible Flat-Plate Boundary Layers

In order to test the  $k-\omega$  model for effects of compressibility, we consider flows 8101 and 8201 of the second Stanford conference.<sup>11</sup> We first consider the adiabatic-wall case with freestream Mach number 0-5. For each Mach number, computation begins at an  $Re_x$  of  $1.0 \cdot 10^6$  and continues to the point where momentum-thickness Reynolds number  $Re_\theta$  is 10,000. Figure 7a compares the computed ratio of skin friction  $C_f$  to the incompressible value  $C_{f0}$ , with the correlation developed by Rubesin. As shown, differences between computed ratios and correlated values are barely noticeable.

Next, we turn to effects to surface temperature on flat-plate skin friction. For this round of computations, the freestream Mach number is 5; the ratio of surface temperature to the adiabatic-wall value ranges from 0.2 to 1.0. Again, computation begins at  $Re_x = 1.0 \cdot 10^6$  and terminates when  $Re_\theta = 10,000$ . Figure 7b compares the predicted ratio of  $C_f$  to the incompressible value with Rubesin's correlation for the range of surface temperatures considered. Differences between predicted and correlated values nowhere exceed 4%.

#### C. Incompressible Free Shear Flows

The final application is to an incompressible free shear flow, specifically, to the mixing layer. The model equations admit a similarity solution in which the independent variable is  $\eta = y/x$ . To solve the resulting equations, we have used the same time-marching procedure implemented in the defect-layer and sublayer analyses of Secs. III and IV. Complete analytical and numerical details are given by Wilcox.<sup>28</sup>

To compare computed and measured spreading rates, we use the definition given by Birch in the second Stanford conference.<sup>11</sup> Predicted spreading rate is sensitive to the freestream values of  $k$  and  $\omega$ , so that a range of spreading rates between 0.100 and 0.141 is possible. This range brackets the measured value of 0.115.

## VI. Summary and Conclusions

The primary objectives of this study have been accomplished: we have made a critical review of closure approximations used in two-equation turbulence models and determined what appears to be an optimum choice of dependent variables. As a result, we have developed a new two-equation model that promises more accuracy for boundary layers in an adverse pressure gradient than any similar model.

As in our prior turbulence modeling efforts, we have made extensive use of perturbation methods (Secs. III and IV). In contrast to prior studies, our analysis of the defect layer includes pressure gradient. As discussed in Sec. III, limiting the defect-layer analysis to the constant-pressure case displays little difference among the various two-equation models in general usage. However, as soon as an adverse pressure gradient is included, the models exhibit large differences. As a general observation, the second Stanford conference demonstrated that modern turbulence models are not much more accurate than those in use in 1968 if the flow of concern is a boundary layer in adverse pressure gradient. The analysis of Sec. III indicates why this is true and, with the introduction of the new model, offers the basis for development of new models that are accurate for such flows.

The model thus far has been tested for the mixing layer, four incompressible boundary layers, and effects of compressibility on flat-plate boundary layers. These numerical applications complement the perturbation analysis predictions of this paper and further validate the claim that the  $k-\omega$  model is much more accurate than comparable two-equation models. More testing is needed and will be done in future research efforts.

Additional development of the model will be needed, however, before such tests can or should be done. Most importantly, the constitutive relation between Reynolds stress and mean-flow properties must be revised. Use of the Boussinesq approximation that stress is proportional to strain rate fails both to predict anisotropy of the normal stresses and to account for streamline curvature effects. Additionally, it is not at all clear that model predictions will bear any relation to physical reality for flows that are unsteady and/or include boundary-layer separation.

Although important development work remains to be done, the primary intent of this work has been to settle the issue of the correct scale-determining equation, and the effort has been

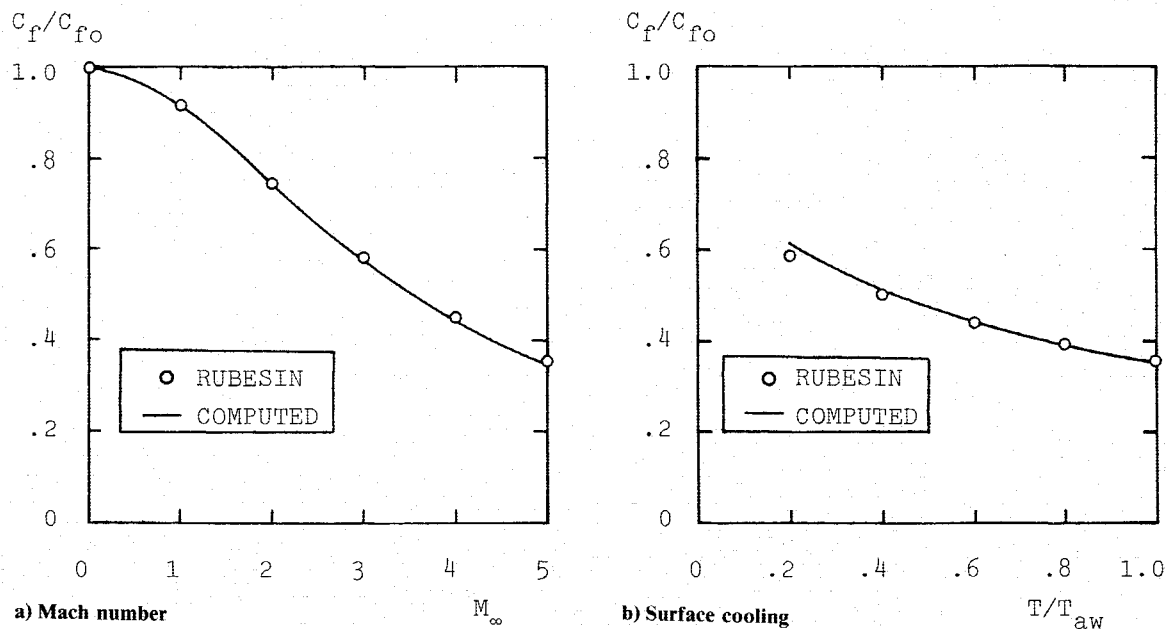


Fig. 7 Comparison of computed and measured effects of freestream Mach number and surface cooling on flat-plate boundary-layer skin friction.

successful. Now that this step has been accomplished, complicating effects such as anisotropic shear, streamline curvature, unsteadiness, and separation can be addressed by building on the solid foundation offered by the  $k$ - $\omega$  model introduced in this paper.

### Appendix: Defect-Layer Equations

In this Appendix, we present details of the formal perturbation expansion solution to the defect-layer equations. First, we summarize the three turbulence models under consideration. Next, we outline the form of the perturbation expansions and state the equations for the leading-order terms in the expansions. Then, we present boundary conditions used in solving the defect-layer equations. Finally, we indicate the manner in which skin friction and wake strength can be extracted from the defect-layer solution.

#### Turbulence Models Under Consideration

In analyzing the defect layer, we focus on three turbulence models: the new model postulated in Sec. II, the Wilcox-Rubesin<sup>10</sup> model, and the Jones-Launder<sup>5</sup> model. For all three of the models, we must solve the equations for mean mass and momentum conservation, an equation for turbulent energy, and an equation for a turbulence dissipation scale. For all three models, the first three equations assume the following form:

$$\frac{\partial u}{\partial x} + \frac{\partial v}{\partial y} = 0 \quad (A1)$$

$$\frac{du}{dt} = U_e \frac{dU_e}{dx} + \frac{\partial}{\partial y} \left[ \nu_T \frac{\partial u}{\partial y} \right] \quad (A2)$$

$$\frac{dk}{dt} = \nu_T \left[ \frac{\partial u}{\partial y} \right]^2 - \epsilon + \frac{\partial}{\partial y} \left[ \sigma^* \nu_T \frac{\partial k}{\partial y} \right] \quad (A3)$$

where  $d/dt = u \partial/\partial x + v \partial/\partial y$ . Note that Eqs. (A1–A3) do not include molecular viscosity. This is a valid approximation in the defect layer as the eddy viscosity is proportional to  $U_e \delta^*$ , where  $U_e$  is the boundary-layer-edge velocity and  $\delta^*$  is displacement thickness. Hence, the ratio of molecular to eddy viscosity varies inversely with displacement-thickness Reynolds number and is thus very small. The difference among the three models is in the way the dissipation  $\epsilon$  and the kinematic eddy viscosity  $\nu_T$  are computed.

For the new model, in addition to Eqs. (A1–A3), we have

$$\epsilon = \beta^* \omega k \quad (A4a)$$

$$\nu_T = k / \omega \quad (A5a)$$

$$\frac{d\omega}{dt} = \gamma \left[ \frac{\partial u}{\partial y} \right]^2 - \beta \omega^2 + \frac{\partial}{\partial y} \left[ \sigma \nu_T \frac{\partial \omega}{\partial y} \right] \quad (A6a)$$

$$\gamma = 5/9, \quad \beta = 3/40, \quad \beta^* = 9/100, \quad \sigma = 1/2, \quad \sigma^* = 1/2 \quad (A7a)$$

In the Wilcox-Rubesin model, the additional equations are as follows:

$$\epsilon = \beta^* \omega k \quad (A4b)$$

$$\nu_T = k / \omega \quad (A5b)$$

$$\frac{d\omega^2}{dt} = \gamma \omega \left[ \frac{\partial u}{\partial y} \right]^2 - \left[ \beta + 2\sigma \left( \frac{\partial \ell}{\partial y} \right)^2 \right] \omega^3 + \frac{\partial}{\partial y} \left[ \sigma \nu_T \frac{\partial \omega^2}{\partial y} \right] \quad (A6b)$$

$$\gamma = 10/9, \quad \beta = 3/20, \quad \beta^* = 9/100, \quad \sigma = 1/2, \quad \sigma^* = 1/2 \quad (A7b)$$

where  $\ell = \sqrt{k}/\omega$ .

In the Jones-Launder model, we compute dissipation  $\epsilon$  directly, so that additional equations are

$$\nu_T = \beta^* k^2 / \epsilon \quad (A5c)$$

$$\frac{d\epsilon}{dt} = \beta^* C_1 k \left[ \frac{\partial u}{\partial y} \right]^2 - C_2 \frac{\epsilon^2}{k} + \frac{\partial}{\partial y} \left[ \sigma \nu_T \frac{\partial \epsilon}{\partial y} \right] \quad (A6c)$$

$$\beta^* = 9/100, \quad C_1 = 31/20, \quad C_2 = 2, \quad \sigma = 10/13, \quad \sigma^* = 1 \quad (A7c)$$

#### Expansion Procedure

Following the formulation of Wilcox and Traci,<sup>9</sup> we introduce a stream function  $\psi$  and seek a perturbation solution of the form

$$\psi = U_e \Delta \left[ \eta - \frac{u_r}{U_e} F_1(\eta) + \dots \right] \quad (A8)$$

$$k = \frac{u_r^2}{\sqrt{\beta^*}} [K_0(\eta) + \dots] \quad (A9)$$

$$\omega = \frac{u_r}{\sqrt{\beta^*} \Delta} [W_0(\eta) + \dots] \quad (A10)$$

$$\epsilon = \frac{u_r^3}{\Delta} [E_0(\eta) + \dots] \quad (A11)$$

where

$$\eta = \frac{y}{\Delta}, \quad \Delta = \frac{U_e \delta^*}{u_r} \quad (A12)$$

Inserting Eqs. (A8–A12) into Eqs. (A1–A7), neglecting higher-order terms, letting  $N_0(\eta)$  denote dimensionless eddy viscosity, and defining

$$U_1(\eta) = \frac{\partial F_1}{\partial \eta}, \quad L_0(\eta) = \frac{\sqrt{K_0}}{W_0} \quad (A13)$$

we obtain the following equations:

$$\begin{aligned} \frac{\partial}{\partial \eta} \left[ N_0 \frac{\partial U_1}{\partial \eta} \right] + (\alpha_T - 2\beta_T - 2\omega_T) \eta \frac{\partial U_1}{\partial \eta} \\ + (\beta_T - 2\omega_T) U_1 = 2\sigma_T x \frac{\partial U_1}{\partial x} \end{aligned} \quad (A14)$$

$$\begin{aligned} \sigma^* \frac{\partial}{\partial \eta} \left[ N_0 \frac{\partial K_0}{\partial \eta} \right] + (\alpha_T - 2\beta_T - 2\omega_T) \eta \frac{\partial K_0}{\partial \eta} - 4\omega_T K_0 \\ + \sqrt{\beta^*} \left[ N_0 \left( \frac{\partial U_1}{\partial \eta} \right)^2 - E_0 \right] = 2\sigma_T x \frac{\partial K_0}{\partial x} \end{aligned} \quad (A15)$$

where

$$E_0 = K_0 W_0 \quad \text{and} \quad N_0 = \frac{K_0}{W_0} = \frac{K_0^2}{E_0} \quad (A16)$$

The final equation for each model is different; the equations are:

New model:

$$\begin{aligned} \sigma \frac{\partial}{\partial \eta} \left[ N_0 \frac{\partial W_0}{\partial \eta} \right] + (\alpha_T - 2\beta_T - 2\omega_T) \eta \frac{\partial W_0}{\partial \eta} \\ + (\alpha_T - \beta_T - 4\omega_T) W_0 + \sqrt{\beta^*} \left[ \gamma \left( \frac{\partial U_1}{\partial \eta} \right)^2 - \left( \frac{\beta}{\beta^*} \right) W_0^2 \right] \\ = 2\sigma_T x \frac{\partial W_0}{\partial x} \end{aligned} \quad (A17a)$$

Wilcox-Rubesin model:

$$\begin{aligned} \sigma \frac{\partial}{\partial \eta} \left[ N_0 \frac{\partial W_0^2}{\partial \eta} \right] + (\alpha_T - 2\beta_T - 2\omega_T)\eta \frac{\partial W_0^2}{\partial \eta} \\ + 2(\alpha_T - \beta_T - 4\omega_T)W_0^2 + \sqrt{\beta^*} \left\{ \gamma W_0 \left( \frac{\partial U_1}{\partial \eta} \right)^2 \right. \\ \left. - \left[ \frac{\beta}{\beta^*} + 2\sigma \left( \frac{\partial L_0}{\partial \eta} \right)^2 \right] W_0^3 \right\} = 2\sigma_T x \frac{\partial W_0^2}{\partial x} \end{aligned} \quad (A17b)$$

Jones-Launder model:

$$\begin{aligned} \sigma \frac{\partial}{\partial \eta} \left[ N_0 \frac{\partial E_0}{\partial \eta} \right] + (\alpha_T - 2\beta_T - 2\omega_T)\eta \frac{\partial E_0}{\partial \eta} \\ + (\alpha_T - \beta_T - 8\omega_T)E_0 + \sqrt{\beta^*} \left[ \frac{C_1}{\beta^*} K_0 \left( \frac{\partial U_1}{\partial \eta} \right)^2 \right. \\ \left. - C_2 \frac{E_0^2}{K_0} \right] = 2\sigma_T x \frac{\partial E_0}{\partial x} \end{aligned} \quad (A17c)$$

where the parameters  $\alpha_T$ ,  $\beta_T$ ,  $\sigma_T$ , and  $\omega_T$  are defined in terms of  $\delta^*$ ,  $u_\tau$ , and skin friction,  $C_f = 2(u_\tau/U_e)^2$ , i.e.,

$$\begin{aligned} \alpha_T &= \frac{2}{C_f} \frac{d\delta^*}{dx} \\ \beta_T &= \frac{\delta^*}{\tau_w} \frac{dp}{dx} \\ \sigma_T &= \frac{\delta^*}{C_f x} \\ \omega_T &= \frac{\delta^*}{C_f u_\tau} \frac{du_\tau}{dx} \end{aligned} \quad (A18)$$

Equations (A14–A17) will have self-similar solutions only if  $\alpha_T$ ,  $\beta_T$ , and  $\omega_T$  are independent of  $x$ . As noted by Bush and Fendell,<sup>16</sup> for  $(U_e \delta^*/\nu) \gg 1$ ,  $u_\tau$  varies sufficiently slowly that we have

$$\omega_T = o(1) \quad \text{as} \quad U_e \delta^*/\nu \rightarrow \infty \quad (A19)$$

and, in addition, the shape factor to leading order approaches 1, which (from inspection of the momentum-integral equation) implies

$$\alpha_T - 1 + 3\beta_T \quad \text{as} \quad U_e \delta^*/\nu \rightarrow \infty \quad (A20)$$

Thus, self-similar solutions exist, provided only that  $\beta_T$  is independent of  $x$ .

In summary, the defect-layer equations for the leading-order terms in the perturbation expansions become

All models:

$$\frac{d}{d\eta} \left[ N_0 \frac{dU_1}{d\eta} \right] + (1 + \beta_T)\eta \frac{dU_1}{d\eta} + \beta_T U_1 = 0 \quad (A21)$$

$$\begin{aligned} \sigma^* \frac{d}{d\eta} \left[ N_0 \frac{dK_0}{d\eta} \right] + (1 + \beta_T)\eta \frac{dK_0}{d\eta} \\ + \sqrt{\beta^*} \left[ N_0 \left( \frac{dU_1}{d\eta} \right)^2 - E_0 \right] = 0 \end{aligned} \quad (A22)$$

New model:

$$\begin{aligned} \sigma \frac{d}{d\eta} \left[ N_0 \frac{dW_0}{d\eta} \right] + (1 + \beta_T)\eta \frac{dW_0}{d\eta} + (1 + 2\beta_T)W_0 \\ + \sqrt{\beta^*} \left[ \gamma \left( \frac{dU_1}{d\eta} \right)^2 - \frac{\beta}{\beta^*} W_0^2 \right] = 0 \end{aligned} \quad (A23a)$$

Wilcox-Rubesin model:

$$\begin{aligned} \sigma \frac{d}{d\eta} \left[ N_0 \frac{dW_0^2}{d\eta} \right] + (1 + \beta_T)\eta \frac{dW_0^2}{d\eta} + 2(1 + 2\beta_T)W_0^2 \\ + \sqrt{\beta^*} \left\{ \gamma W_0 \left( \frac{dU_1}{d\eta} \right)^2 - \left[ \frac{\beta}{\beta^*} + 2\sigma \left( \frac{dL_0}{d\eta} \right)^2 \right] W_0^3 \right\} = 0 \end{aligned} \quad (A23b)$$

Jones-Launder model:

$$\begin{aligned} \sigma \frac{d}{d\eta} \left[ N_0 \frac{dE_0}{d\eta} \right] + (1 + \beta_T)\eta \frac{dE_0}{d\eta} + (1 + 2\beta_T)E_0 \\ + \sqrt{\beta^*} \left[ \frac{C_1}{\beta^*} K_0 \left( \frac{dU_1}{d\eta} \right)^2 - C_2 \frac{E_0^2}{K_0} \right] = 0 \end{aligned} \quad (A23c)$$

#### Boundary Conditions

At the outer edge of the defect layer, we require that the velocity equal the freestream velocity. Additionally, we let the turbulent energy assume a small value and insist that the turbulent length scale have zero slope at the boundary-layer edge. In their defect-layer analysis, Wilcox and Traci used these boundary conditions, as well as explicitly prescribing both  $K_0$  and  $W_0$ . Thus,

$$U_1 = \frac{dL_0}{d\eta} = 0 \quad \text{and} \quad K_0 = \text{small value} \quad \text{at} \quad \eta = \eta_e \quad (A24)$$

Approaching the surface, we must formally match to the law of the wall. Matching is a bit different for each model but is nevertheless straightforward; details of the algebra will thus be omitted in the interest of brevity. The limiting forms used for  $\eta \rightarrow 0$  follow.

$$\left. \begin{aligned} U_1 &\sim \frac{1}{\kappa} [-\ell \eta + u_0 - u_1 \eta \ell \eta] \\ K_0 &\sim [1 + k_1 \eta \ell \eta] \\ W_0 &\sim \frac{1}{\kappa \eta} [1 + w_1 \eta \ell \eta] \\ E_0 &\sim \frac{1}{\kappa \eta} [1 + e_1 \eta \ell \eta] \end{aligned} \right\} \quad \text{as} \quad \eta \rightarrow 0 \quad (A25)$$

The coefficients  $u_1$ ,  $k_1$ ,  $w_1$ , and  $e_1$  are as follows:

All models:

$$k_1 = \frac{\beta_T/\kappa}{\sigma^* \kappa^2/(2\sqrt{\beta^*}) - 1} \quad (A26)$$

New model:

$$u_1 = \frac{[\beta/(\gamma\beta^*)] \sigma^* \kappa^2/(2\sqrt{\beta^*})}{1 - \beta/(\gamma\beta^*)} k_1 \quad (A27a)$$

$$w_1 = \frac{\sigma^* \kappa^2/(2\sqrt{\beta^*})}{1 - \beta/(\gamma\beta^*)} k_1 \quad (A28a)$$

Wilcox-Rubesin model:

$$u_1 = \frac{[\beta/\sqrt{\beta^*} + \sigma\kappa^2] \sigma^* \kappa^2 / (2\sqrt{\beta^*})}{2\gamma\sqrt{\beta^*} [1 - \beta/(\gamma\beta^*)] + 2\sigma\kappa^2} k_1 \quad (\text{A27b})$$

$$w_1 = \frac{\gamma\sqrt{\beta^*} [\sigma^* \kappa^2 / (2\sqrt{\beta^*})] + \sigma\kappa^2}{2\gamma\sqrt{\beta^*} [1 - \beta/(\gamma\beta^*)] + 2\sigma\kappa^2} k_1 \quad (\text{A28b})$$

Jones-Launder model:

$$u_1 = \frac{(1 + \sigma^* \kappa^2 / \sqrt{\beta^*}) C_2 - C_1}{2(C_1 - C_2)} k_1 \quad (\text{A27c})$$

$$e_1 = \frac{(1 + \sigma^* \kappa^2 / \sqrt{\beta^*}) C_1 - C_2}{2(C_1 - C_2)} k_1 \quad (\text{A28c})$$

Additionally, the coefficient  $u_0$  is determined from the integral constraint for mass conservation, that is,

$$\int_0^{\eta_e} U_1(\eta) d\eta = 1 \quad (\text{A29})$$

To implement Eq. (A29) in the numerical solution of the defect-layer equations, we proceed as follows. Because the velocity is singular at  $\eta = 0$ , we integrate the numerical velocity profile from a point above the surface, which we denote by  $\eta_L$  (typically of order 0.001–0.01), to the edge of the boundary layer  $\eta_e$ . Then, we integrate the asymptotic profile for  $U_0(\eta)$  given in Eqs. (A25) from  $\eta = 0$  to  $\eta = \eta_L$ . The latter integration involves the unknown coefficient  $u_0$ . Finally, the sum of these two integrals must be unity by virtue of Eq. (A29).

#### Skin Friction and Wake Strength

It is possible to determine the skin friction implied by the solution to the defect-layer equations by formal matching to the sublayer asymptotic velocity profile. Considering only leading-order terms, we say:

$$\lim_{y^+ \rightarrow \infty} \left[ \frac{1}{\kappa} \ln y^+ + B \right] = \lim_{\eta \rightarrow 0} \left[ \frac{U_e}{u_\tau} + \frac{1}{\kappa} \ln \eta - \frac{1}{\kappa} u_0 \right] \quad (\text{A30})$$

We note that  $y^+ = \eta / (U_e \delta^* / \nu)$  and  $u_\tau / U_e = \sqrt{C_f / 2}$ , there follows immediately:

$$\sqrt{\frac{C_f}{2}} = B + \frac{1}{\kappa} u_0 + \frac{1}{\kappa} \ln \left( \frac{U_e \delta^*}{\nu} \right) \quad (\text{A31})$$

Finally, combining Coles' composite profile [Eq. (22)] with Eq. (A31) and evaluating the resulting equation at the boundary-layer edge, we arrive at the following expression for wake strength  $\tilde{\pi}$ .

$$\tilde{\pi} = \frac{1}{2} (u_0 - \ln \eta_e) \quad (\text{A32})$$

#### Acknowledgment

This research was sponsored by the U.S. Army Research Office under Contract DAAG-29-83-C-0003 with Dr. Robert E. Singleton as technical monitor.

#### References

- <sup>1</sup>Cebeci, T. and Smith, A. M. O., *Analysis of Turbulent Boundary Layers*, Series in Applied Mathematics and Mechanics, Vol. XV, Academic Press, Orlando, FL, 1974.
- <sup>2</sup>Coles, D. E. and Hirst, E. A., *Computation of Turbulent Boundary Layers—1968 AFOSR-IFP-Stanford Conference*, Vol. II, Stanford Univ. Press, Stanford, CA, 1969.
- <sup>3</sup>Bradshaw, P., Ferriss, D. H., and Atwell, N. P., "Calculation of Boundary Layer Development Using the Turbulent Energy Equation," *Journal of Fluid Mechanics*, Vol. 28, Pt. 3, 1967, pp. 593–616.
- <sup>4</sup>Donaldson, C. duP., "Calculation of Turbulent Shear Flows for Atmospheric and Vortex Motions," *AIAA Journal*, Vol. 10, Jan. 1972, pp. 4–12.
- <sup>5</sup>Jones, W. P. and Launder, B. E., "The Prediction of Laminarization with a Two-Equation Model of Turbulence," *International Journal of Heat and Mass Transfer*, Vol. 15, 1972, pp. 301–314.
- <sup>6</sup>Rodi, W., "Progress in Turbulence Modeling for Incompressible Flows," AIAA Paper 81-0045, Jan. 1981.
- <sup>7</sup>Wilcox, D. C. and Alber, I. E., "A Turbulence Model for High Speed Flows," *Proceedings of the 1972 Heat Transfer and Fluid Mechanics Institute*, Stanford Univ. Press, Stanford, CA, 1972, pp. 231–252.
- <sup>8</sup>Saffman, P. G. and Wilcox, D. C., "Turbulence-Model Predictions for Turbulent Boundary Layers," *AIAA Journal*, Vol. 12, April 1974, pp. 541–546.
- <sup>9</sup>Wilcox, D. C. and Traci, R. M., "A Complete Model of Turbulence," AIAA Paper 76-351, July 1976.
- <sup>10</sup>Wilcox, D. C. and Rubesin M. W., "Progress in Turbulence Modeling for Complex Flow Fields Including Effects of Compressibility," NASA TP-1517, April 1980.
- <sup>11</sup>Kline, S. J., Cantwell, B. J., and Lilley, G. M. (eds.), *Proceedings of the 1980-81 AFOSR-HTTM-Stanford Conference on Complex Turbulent Flows*, Stanford Univ. Press, Stanford, CA, 1981.
- <sup>12</sup>MacCormack, R. W., "A Numerical Method for Solving the Equations of Compressible Viscous Flow," AIAA Paper 81-0110, Jan. 1981.
- <sup>13</sup>Favre, A., "Equations des Gaz Turbulents Compressibles," *Journal de Mécanique*, Vol. 4, No. 3, 1965, pp. 361–390.
- <sup>14</sup>Kolmogorov, A. N., "Equations of Turbulent Motion of an Incompressible Fluid," *Izvestia Academy of Sciences, USSR; Physics*, Vol. 6, Nos. 1 and 2, 1942, pp. 56–58.
- <sup>15</sup>Townsend, A. A., *The Structure of Turbulent Shear Flow*, 2nd ed., Cambridge University Press, Cambridge, England, 1976, pp. 107–108.
- <sup>16</sup>Bush, W. B. and Fendell, F. E., "Asymptotic Analysis of Turbulent Channel and Boundary-Layer Flow," *Journal of Fluid Mechanics*, Vol. 56, Pt. 4, 1972, pp. 657–681.
- <sup>17</sup>Chambers, T. L. and Wilcox, D. C., "Critical Examination of Two-Equation Turbulence Closure Models for Boundary Layers," *AIAA Journal*, Vol. 15, July 1977, pp. 821–828.
- <sup>18</sup>Laufer, J., "The Structure of Turbulence in Fully Developed Pipe Flow," NACA 1174, 1952.
- <sup>19</sup>Andersen, P. S., Kays, W. M., and Moffat, R. J., "The Turbulent Boundary Layer on a Porous Plate: An Experimental Study of the Fluid Mechanics for Adverse Free-Stream Pressure Gradients," Dept. of Mechanical Engineering, Stanford University, Stanford, CA, Rept. HMT-15, May 1972.
- <sup>20</sup>Saffman, P. G., "A Model for Inhomogeneous Turbulent Flow," *Proceedings of the Royal Society, London*, Vol. A317, 1970, pp. 417–433.
- <sup>21</sup>Schlichting, H., *Boundary Layer Theory*, 4th ed., McGraw-Hill, New York, 1960, pp. 519–527.
- <sup>22</sup>Wilcox, D. C. and Chambers, T. L., "Further Refinement of the Turbulence Model Transition-Prediction Technique," DCW Industries, Sherman Oaks, CA, Rept. DCW-R-03-02, 1975.
- <sup>23</sup>Wilcox, D. C., "Program EDDYBL User's Guide," DCW Industries, La Cañada, CA, Rept. DCW-R-NC-04, 1988.
- <sup>24</sup>Blottner, F. G., "Variable Grid Scheme Applied to Turbulent Boundary Layers," *Computational Methods for Applied Mechanics and Engineering*, Vol. 4, No. 2, 1974, pp. 179–194.
- <sup>25</sup>Wilcox, D. C., "Algorithm for Rapid Integration of Turbulence Model Equations on Parabolic Regions," *AIAA Journal*, Vol. 19, Feb. 1981, pp. 248–251.
- <sup>26</sup>Wilcox, D. C., "A Complete Model of Turbulence Revisited," AIAA Paper 84-0176, Jan. 1984.
- <sup>27</sup>Rodi, W. and Scheuerer, G., "Scrutinizing the  $k-\epsilon$  Turbulence Model Under Adverse Pressure Gradient Conditions," *Transactions of the ASME*, Vol. 108, June 1986, pp. 174–179.
- <sup>28</sup>Wilcox, D. C., "More Advanced Applications of the Multiscale Model for Turbulent Flows," AIAA Paper 88-0220, Jan. 1988.